ORIGINAL ARTICLE

Numerical Study of Thermocapillary-Buoyancy Convection of Volatile Liquid Layer in an Enclosed Cavity

Guofeng Xu [1,2] · Qiusheng Liu [1,2] (iD) · Jun Qin [1,2] · Zhi-Qiang Zhu [1]

Abstract

In this paper, steady thermocapillary-buoyancy convection of a volatile liquid layer in the case of a two-dimensional enclosed cavity subjected to horizontal temperature gradient is numerically investigated by using the finite difference method. A two-phase model with convective diffusion of vapor in consideration is fully developed. Kinetic theory of gases and vapor-diffusion-limited phase change are used to describe mass flux on the liquid-gas interface, and the latter is validated to play a dominating role in phase change. Numerical results reveal that transition from unicellular flow to multicellular flow in liquid layer is due to the increasing thermocapillary effect, while increasing buoyancy effect has a major impact on gas flow, which can separate the convection in gas phase into a two-layer flow. Evaporation and condensation occur at the interface and the mass flux distribution is bound up with the convective patterns in liquid layer. For a large imposed temperature gradient, the interfacial mass flux fluctuates in the core region with its amplitudes gradually amplifying from the cold to hot side. Thermal boundary effect on temperature and mass flux distribution close to the end walls is discussed. We also simulate a corresponding model ignoring phase change and vapor transport, and find the phase change tends to stabilize the thermocapillary-buoyancy flows due to the reduction of interfacial temperature gradient caused by the latent heat absorbed and released along the interface.

Introduction

Natural thermo-convection in a liquid layer driven by thermocapillary and buoyancy effects has been systematically studied during the last few decades, initially due to the great importance in industrial and scientific applications, such as crystal growth, two-phase capillary pumped loops and microgravity thermal management devices (Derby 2016; Chen and Lin 2001; Abe et al. 2005). Bénard (1900) was the first to find the convective flow patterns in a very thin liquid layer which is referred to as Rayleigh-Bénard convection, thereafter, a new theoretical model was proposed by Pearson (1958) that it is the temperature-gradient-induced variation of surface tension

stirs up the liquid and forms the convection which is named Marangoni-Bénard convection. Nield (1964) integrated both the Marangoni and buoyancy effects to demonstrate the onset of convection, called thermocapillary-buoyancy convection.

Not only the convections, but a different mode of instability referred to as hydrothermal waves in an infinite liquid layer bounded with horizontal temperature gradient was first predicted by Smith and Davis (1983) using a linear stability analysis. It was then observed and confirmed in the experiment performed by Riley and Neitzel (1998). For a thin liquid layer (O(1 mm)) with a moderate Prandtl number (O(10)), thermal waves obliquely propagate from the cold to the hot end, but for a thicker liquid layer, a transition from the steady return-flow basic state to the oscillatory state with the increasing Marangoni number was found instead of the hydrothermal waves. Simanovskii et al. (2018) investigated the thermocapillary-buoyancy convection in a laterally heated two-layer system using nonlinear simulation. Mo and Ruan (2019) performed a linear-stability analysis to study the thermocapillary-buoyancy convection in an annular two-layer system and found the stabilizing effect of buoyancy.

✉ Qiusheng Liu
liu@imech.ac.cn

1   Key Laboratory of Microgravity, Institute of Mechanics, Chinese
Academy of Sciences, Beijing 100190, China

2   University of Chinese Academy of Sciences, Beijing 100049, China

Zhang and Li (2019) numerically investigated the effect of surface heat dissipation on the thermocapillary convection of 0.65 cSt silicone oil in an annular pool. According to these studies, both thermocapillary effect and buoyancy effect can significantly influence the flow structure in a differentially and horizontally heated liquid layer. However, these investigations all omit the phase change occurring at the liquid-gas interface. The natural convection induced by the coupling of phase change, buoyancy effect and thermocapillary effect in a volatile liquid layer has not been well studied. In fact, a wide variety of heat transfer device, such as heat pipes (Cecere et al. 2019) and space thermal management devices (Wang et al. 2015; Zhu et al. 2010; Brutin et al. 2010), take advantage of the large latent heat during the phase-change process to improve the heat dissipation efficiency. Other application like droplet evaporation (Chen et al. 2015, 2017, 2018; Zhang et al. 2019) is also a complex physics coupled by flow motion and phase change. Therefore, convection coupled with the evaporation (condensation) have attracted the theoretical and technological interests in recent years.

Palmer (1976) used linear stability analysis to investigate the instability of rapidly evaporating liquids under the reduced pressure. Differential vapor recoil coupled with the Marangoni effect was fully analyzed. Chai and Zhang (1998) found that evaporation plays an important role in convective instability, which also acts as a convective driving force. Zhu and Liu (2010) conducted an experiment with the volatile 0.65 cSt silicone oil in an open cavity differentially heated at the lateral walls. At the different imposed temperature difference, average interfacial evaporation rate and temperature distribution were measured and three major flow regimes at a streamwise transverse plane were observed. Li et al. (2014) employed the same working liquid as Zhu and Liu (2010) in their experiment, while the cavity (48.5 mm × 10 mm × 10 mm) is sealed at the top. Critical laboratory and interfacial Marangoni numbers at the transition state between different flow patterns were summarized at different air concentration in the gas phase. For the first time, the authors found out that the critical Marangoni numbers of the transition flow states increase with the decreasing of the air concentration, even though the air concentration has little impact on the liquid bulk flow. Based on these previous researches, one can find that gas phase actually plays an important role in the phase change process which has a great impact on the liquid flow due to vapor recoil effect and the latent heat released or absorbed at the interface.

To understand the flow regimes and instability of a liquid layer with phase change, numerical simulations and analytics are essential. However, for most of previous studies (Schmidt et al. 1995; Ji et al. 2008; Zhang et al. 2016), gas phase is ignored and so called "one-sided" model is employed. Liu and Liu (Liu et al. 2005; Liu and Liu 2006) defined a new evaporation Biot number, which is derived from the linearized

Hertz-Knudsen equation (Burelbach et al. 1988), to describe the evaporation intensity in a liquid-layer system heated or cooled at the bottom. In their model, gas phase is completely filled with vapor and the mass flux from phase change is solely determined by the non-equilibrium kinetic theory of gases, which is an ideal state for most of the cooling devices, even though two-sided model taking into account mass and energy balance at the vapor-liquid interface is employed. An improved 1.5-sided model was proposed by Margerit et al. (2005). The gas phase in their model is a component of liquid vapor and inert gas, but the two-phase model is simplified by neglecting convection of gas and Hertz-Knudsen equation in relating interfacial mass flux.

Recently, several direct numerical simulations of a volatile liquid layer differentially heated at the two lateral walls, which used two-sided model by fully accounting for the dynamics of the vapor phase, were conducted. Sáenz et al. (2014) performed a 3D simulation in an open cubic cavity. It was found evaporation has stabilizing effects due to the latent energy that inhibits hydrothermal waves. In particular, Marangoni effect drives the vapor close to the interface move from the hot end to the cold end, the accumulated vapor near the cold wall leads to condensation in a narrow region adjacent to the cold wall. Otherwise, Qin et al. (2014) performed a 2D and 3D simulation in a sealed rectangular cavity. They validated that 2D approximation is reasonably accurate and wetting effect of the lateral walls by the fluid has a minor influence on the simulation results. The authors also validated that one-sided model is quite restrictive. The dynamic Bond number in their simulations is fixed at 0.853, which means thermocapillary effect balances the buoyancy effect. Bekezhanova and Goncharova (2019) numerically studied the 3D thermocapillary convection for liquid-gas system with phase transition in a weak gravity field. The flow structure is found to be influenced by the coupling of thermocapillary convection and phase-change effect. However, as Burguete et al. (2001), Riley and Neitzel (1998) and Chan and Chen (2010) reported, the depth of liquid layer, corresponding to the dynamic Bond number, plays a vital role in flow regimes and instability. Thus, more details of the correlation among the phase change, flow patterns, heat transfer and vapor dynamics need to be further studied, when dynamic Bond number varies.

The present paper aims to investigate the thermo-convection caused by the thermocapillary effect and buoyancy effect in an enclosed cavity subjected to horizontal temperature gradient, where interfacial phase change has a crucial impact mutually. A two-phase mathematical model is developed in Section 2, and its numerical method is presented in Section 3. Results of convective patterns, temperature fields and coupling mechanisms of thermocapillary-buoyancy effect with phase change effect are introduced and discussed in Section 4. Finally, conclusions are summarized in Section 5.
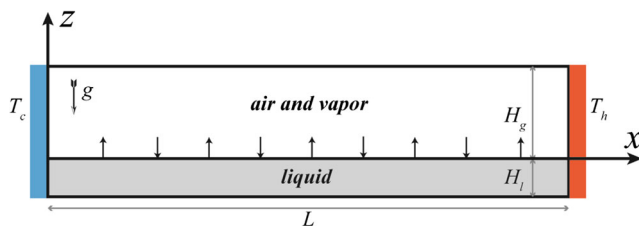
Mathematical Model

Problem Description

A novel physical model is presented in Fig. 1 describing thermocapillary-buoyancy convection in an enclosed cavity with phase change occurring at the liquid-gas interface. The incompressible, Newtonian liquid and gas (component of air and vapor) are contained in a two-dimensional rectangular cavity of height $H = H_l + H_g$ and width L, where the liquid layer aspect ratio is $\Gamma = L/H_l$ and height ratio of gas layer to liquid layer is $\Pi = H_l/H_g$. Here and below, subscripts l, g, v, a, i, c and h denote liquid phase, gas phase, vapor component, air component, liquid-gas interface, cold wall and hot wall, respectively. The lateral walls are rigid, the left wall is cooled on the left side to be at constant temperature T_c, and the right wall is heated on the right side to be at constant temperature T_h.

It's suggested by Qin et al. (2014) that the impact of the contact angle at the triple lines on the flow pattern is relatively weak and can be ignored. Furthermore, as introduced by Liu and Liu (2006), if the capillary number $Ca = \mu_l\alpha_l/\sigma H_l$ is in the limit of zero and the Galileo number $Ga = \rho_l g H_l^2/\sigma$ is in the limit of infinite, where μ is dynamic viscosity, α is the thermal diffusivity and σ is the surface tension, the liquid-gas interface deformation can be neglected. In present model, a corresponding working liquid will be used, hence the interface is considered flat and non-deformable. The thermophysical properties in the liquid and gas phase are assumed to be constant at the reference temperature $T_0 = T_c$ except for the fluid density ρ in the buoyancy terms of the Navier-Stokes equations, in which it varies linearly with the local temperature as $\rho_l = \rho_{l,c}[1 - \beta_l(T - T_c)]$ and $\rho_g = \rho_{g,c}[1 - \beta_g(T - T_c)]$, where β is the coefficient of thermal expansion.

Governing Equations

The height of liquid layer H_l is selected as the length scale and the problem is scaled by H_l^2/ν_l, ν_l/H_l, $\rho_l\nu_l^2/H_l^2$ as units for the time t, velocity vector $\mathbf{u}$ and pressure p, respectively, where ν is the kinematic viscosity. The dimensionless temperature is

Fig. 1 Schematic of the mathematical model. White and grey regions correspond to the gas phase and liquid phase, respectively. Phase change occurs at the gas-liquid interface ($z = 0$). The cavity is enclosed. Here and below, the region in grey (white) represents the liquid (gas) phase

defined as $\Theta = (T - T_c)/\Delta T$, where $\Delta T = T_h - T_c$ is the imposed temperature difference between the hot wall and the cold wall. Two sets of mass conservation, momentum conservation followed by the Boussinesq approximation and energy conservation equations govern the flow and heat transfer in the liquid phase and gas phase.

In the liquid phase, dimensionless governing equations hold:

$$\nabla\cdot\mathbf{u}_l = 0, \tag{1}$$

$$\frac{\partial\mathbf{u}_l}{\partial t} + \mathbf{u}_l\cdot\nabla\mathbf{u}_l = -\nabla p_l + \nabla^2\mathbf{u}_l + \frac{Ra}{Pr}\Theta_l\mathbf{k}, \tag{2}$$

$$\frac{\partial\Theta_l}{\partial t} + \mathbf{u}_l\cdot\nabla\Theta_l = \frac{1}{Pr}\nabla^2\Theta_l, \tag{3}$$

and in the gas phase, the dimensionless governing equations hold:

$$\nabla\cdot\mathbf{u}_g = 0, \tag{4}$$

$$\frac{\partial\mathbf{u}_g}{\partial t} + \mathbf{u}_g\cdot\nabla\mathbf{u}_g = -\frac{1}{\rho^*}\nabla p_g + \nu^*\nabla^2\mathbf{u}_g + \frac{Ra}{Pr}\beta^*\Theta_g\mathbf{k}, \tag{5}$$

$$\frac{\partial\Theta_g}{\partial t} + \mathbf{u}_g\cdot\nabla\Theta_g = \frac{\alpha^*}{Pr}\nabla^2\Theta_g, \tag{6}$$

where $\mathbf{k}$ is the unit vector in the z direction, α is the thermal diffusivity and superscript $*$ denotes the ratio of the physical parameters of the gas to the liquid. $Pr = \nu_l/\alpha_l$ is the Prandtl number, $Ra = g\beta_l\Delta T H_l^3/\nu_l\alpha_l$ is the Rayleigh number and the ratio of the Rayleigh number to the Prandtl number $Gr = Ra/Pr$ is the Grashof number which indicates the ratio of the buoyancy to viscous force acting in the bulk of a fluid.

The gas is considered ideal and a component of air and vapor, and the vapor in the air is assumed to be dilute. The vapor transport in gas is given by the diffusion-convection equation:

$$\frac{\partial Y_v}{\partial t} + \mathbf{u}_g\cdot\nabla Y_v = \frac{\nu^*}{Sc}\nabla^2 Y_v, \tag{7}$$

where Y_v is the mass fraction of vapor, $Sc = \nu_g/D$ is the Schmidt number, which indicates the ratio of the viscous diffusion rate to the mass diffusion rate, and D is the diffusion coefficient of the vapor in air.

Boundary Conditions

At the liquid-gas interface, the surface tension is a linear function of the temperature T, $\sigma = \sigma_0 - \sigma_T(T - T_0)$, where σ_0 is the surface tension at the reference temperature $T_0 (T_0 = T_c)$ and $\sigma_T = -\partial\sigma/\partial T$ is surface tension coefficient which is constant and positive. No-slip condition of the velocity in the tangential direction is given by

$$\mathbf{u}_l\cdot\boldsymbol{\tau} = \mathbf{u}_g\cdot\boldsymbol{\tau}, \tag{8}$$

and the mass conservation across the interface leads to

$$E_j = (\mathbf{u}_l - \mathbf{u}_i) \cdot \mathbf{n} = \rho^* (\mathbf{u}_g - \mathbf{u}_i) \cdot \mathbf{n}, \tag{9}$$

where $\mathbf{n}$ and $\boldsymbol{\tau}$ are the unit normal and tangential vector to the interface respectively, j is the dimensionless local mass flux scaled by $k_l \Delta T / H_l \mathcal{L}$, in which $\mathcal{L}$ is the latent heat and k is the thermal conductivity, and $E = k_l \Delta T / \rho_l \nu_l \mathcal{L}$ is the dimensionless evaporation number (Burelbach et al. 1988) which indicates the ratio of phase-change rate to viscous diffusion rate. Specially, due to the assumption of non-deformable interface, the interfacial velocity $\mathbf{u}_i$ is considered a zero vector.

The condition of tangential stress balance at the interface gives

$$\left[\mathbf{n} \cdot \left(\nabla \mathbf{u}_l + (\nabla \mathbf{u}_l)^T \right) - \mu^* \mathbf{n} \cdot \left(\nabla \mathbf{u}_g + (\nabla \mathbf{u}_g)^T \right) \right] \cdot \boldsymbol{\tau}$$
$$= -\frac{\mathrm{Ma}}{\mathrm{Pr}} \nabla \Theta_i \cdot \boldsymbol{\tau}, \tag{10}$$

where Ma is the dimensionless Marangoni number defined as

$$\mathrm{Ma} = \frac{\sigma_T \Delta T H_l}{\mu_l \alpha_l}. \tag{11}$$

Since the interface is flat, the normal stress balance at the interface does not need to be considered.

The temperature at the liquid-gas interface is continuous,

$$\Theta_l = \Theta_g = \Theta_i, \tag{12}$$

but the heat flux is discontinuous due to the latent heat absorbed in liquid vaporization and released in vapor condensation, the energy balance gives

$$j = -\nabla \Theta_l \cdot \mathbf{n} + k^* \nabla \Theta_g \cdot \mathbf{n}. \tag{13}$$

A kinetic theory of mass balance at the liquid–gas interface proposed by Schrage (1953) is used to describe the dimensional vapor mass flux j_m

$$j_m = \frac{2\lambda}{2-\lambda} \sqrt{\frac{M_v}{2\pi \overline{R}}} \left[P_{g,t} \left(\frac{\overline{p}_{sat}(\Theta_i)}{\sqrt{T_i}} - \frac{\overline{p}_v(Y_v)}{\sqrt{T_g}} \right) \right], \tag{14}$$

where λ is the accommodation coefficient, which is taken to equal 0.1, M_v is the molecular weight, $\overline{R} = 8.314 \text{ J/(mol·K)}$ is the universal gas constant and $P_{g,t}$ is the dimensional total pressure at the top of gas layer. $\overline{p}_{sat}(\Theta_i)$ is the dimensionless interfacial saturation vapor pressure which can be computed using the Clausius-Clapeyron relation

$$\overline{p}_{sat}(\Theta_i) = \frac{P_{v,0}}{P_{g,t}} \exp \left[-\frac{M_v \mathcal{L}}{\overline{R}} \left(\frac{1}{T_c + \Theta_i \Delta T} - \frac{1}{T_0} \right) \right], \tag{15}$$

where $P_{v,0}$ is the dimensional reference saturation vapor pressure at the reference temperature T_0. Particularly, $\overline{p}_{sat}(\Theta_i)$ and

$\overline{p}_v(Y_v)$ are another alternative dimensionless pressure scaled by $P_{g,t}$ (not by $\rho_l \nu_l^2 / H_l^2$).

In gas, each component is ideal,

$$c_v = \frac{p_v}{\overline{R}T}, c_a = \frac{p_a}{\overline{R}T}, \tag{16}$$

where $c = \rho/M$ is the molar concentration and the mass fraction of each component is defined as

$$Y_v = \frac{\rho_v}{\rho_g}, Y_a = \frac{\rho_a}{\rho_g}, \tag{17}$$

the total pressure of gas phase is equal to the sum of the partial pressures of the individual components according to the Dalton's law

$$p_g = p_v + p_a. \tag{18}$$

Combining Eqs. (16)–(18) with

$$X_v = \frac{p_v}{p_g}, \tag{19}$$

the molar fraction of vapor X_v can de related with mass fraction of vapor,

$$X_v = \frac{Y_v}{Y_v + r(1-Y_v)}, \tag{20}$$

where $r = M_v/M_a$ is the molecular weight ratio of vapor to air. Thus, the partial pressure of vapor is computed by

$$p_v(Y_v) = p_g \frac{Y_v}{Y_v + r(1-Y_v)}, \tag{21}$$

which can be written in an alternative dimensionless form as

$$\overline{p}_v(Y_v) = \frac{Y_v}{Y_v + r(1-Y_v)}. \tag{22}$$

The vapor deviates from the interface by means of diffusion and convection, the following vapor mass conservation at the interface holds:

$$E_j = -\frac{\rho^* \nu^*}{\mathrm{Sc}} \nabla Y_v \cdot \mathbf{n} + \rho^* Y_v (\mathbf{u}_g \cdot \mathbf{n} - \mathbf{u}_i \cdot \mathbf{n}). \tag{23}$$

It is assumed that air is immiscible in water, therefore the mass flux of dry air j_a, across the interface is zero

$$E_{j_a} = -\frac{\rho^* \nu^*}{\mathrm{Sc}} \frac{D_a}{D} \nabla Y_a \cdot \mathbf{n} + \rho^* Y_a (\mathbf{u}_g \cdot \mathbf{n} - \mathbf{u}_i \cdot \mathbf{n}) = 0, \tag{24}$$

where D_a is the diffusion coefficient of air in vapor, which is equal to that of vapor in air for a binary mixture,

$$D = D_a. \tag{25}$$

Since we have assumed that the gas phase is incompressible, therefore

$$\rho_g = \rho_v + \rho_a = const, \quad (26)$$

$$Y_v + Y_a = 1. \quad (27)$$

Substituting Eqs. (24), (25) and (27) into Eq. (23) yields

$$Ej = -\frac{\rho^* \nu^*}{Sc} \frac{\nabla Y_v \cdot \mathbf{n}}{1 - Y_v}. \quad (28)$$

Combining Eqs. (12), (14), (15) and (22) yields

$$QEj = \frac{P_{v,0}}{P_{g,t}} \exp\left[-\frac{M_v \mathcal{L}}{\overline{R}}\left(\frac{1}{T_c + \Theta_i \Delta T} - \frac{1}{T_0}\right)\right] - \frac{Y_v}{Y_v + r(1 - Y_v)}, \quad (29)$$

where Q is a dimensionless number (Haut and Colinet 2005) that indicates the resistance to phase change caused by interfacial non equilibrium and defined as

$$Q = \frac{(2-\lambda)\rho_l \nu_l}{2\lambda P_{g,t} H_l} \sqrt{\frac{2\pi \overline{R} T_i}{M_v}}. \quad (30)$$

The average heat flux at the cold and hot walls is characterized by dimensionless Nusselt numbers as

$$Nu_c = \int_{-1}^{\Pi} -\nabla \Theta(0, z) \cdot \mathbf{n} dz, \quad (31)$$

$$Nu_h = \int_{-1}^{\Pi} -\nabla \Theta(\Gamma, z) \cdot \mathbf{n} dz. \quad (32)$$

The remaining boundary conditions for $\mathbf{u}$, Θ and Y_v are listed as follows:

At the bottom of the liquid layer ($z = -1$), no slip condition for $\mathbf{u}_l$ and adiabatic condition for Θ_l hold

$$\mathbf{u}_l = 0, \nabla \Theta_l \cdot \mathbf{n} = 0. \quad (33)$$

At the top of the gas layer ($z = 3$), no slip condition for $\mathbf{u}_g$, adiabatic condition for Θ_g and no penetration condition for Y_v hold

$$\mathbf{u}_g = 0, \nabla \Theta_g \cdot \mathbf{n} = 0, \nabla Y_v \cdot \mathbf{n} = 0. \quad (34)$$

Similarly, inside of the cold and hot walls, no slip and penetration conditions hold

$$\mathbf{u}_l = 0, \mathbf{u}_g = 0, \nabla Y_v \cdot \mathbf{n} = 0. \quad (35)$$

In order to simulate the authentic physical model, we consider the lateral walls with thickness d_w and thermal conductivity k_w. At the outside of the cold and hot walls, temperature is maintained at T_c and T_h, respectively. It is assumed that the walls are thin and made of metal, and timescale of the heat diffusion in the walls is far less than that in the fluid ($d_w^2/\alpha_w \ll H_l^2/\alpha_l$), then quasi-static one-dimensional heat conduction model is used to calculate the temperature distribution inside both walls:

$$\nabla \Theta_c \cdot \mathbf{n} - Bi_{w,j} \Theta_c = 0, \quad (36)$$

$$\nabla \Theta_h \cdot \mathbf{n} + Bi_{w,j}(\Theta_c - 1) = 0, \quad (37)$$

where $Bi_{w,j} = k_w H_l / d_w k_j$, in which $j = l$ ($j = g$) for liquid layer (gas layer), is the dimensionless wall Biot number indicating the heat conduction capacity ratio of the wall to the fluid.

Numerical Method

The governing equations in both liquid and gas phases along with the boundary conditions are solved based on the finite difference method. Fully second order accurate projection method (Liu et al. 2004) is used to decouple the computation of pressure from velocity in the Navier-Stokes equations, leading to a pressure Poisson equation at each time step which is solved by Fourier analysis-cyclic reduction algorithm (FACR) (Swarztrauber 1977). The diffusion terms are discretized by the Crank-Nicolson scheme, the convective terms are discretized by the Adams-Bashforth scheme and all the spatial derivatives are discretized by standard central finite difference. In addition, second-order accurate discretization is employed for the boundary conditions. Steady solutions, if they exist, are obtained when the relative variation of the primitive variables is less than 10^{-6} in a marching time step (2×10^{-5} is used for the basic calculations).

The grid-dependency is checked for four stretched and staggered grids $Nx \times (Nz_l + Nz_g)$, where Nx and Nz are numbers of grids in the x and z direction, respectively. Typical results at Pr = 6.83, Ma = 11880, Gr = 995, Sc = 0.6 and E = 3.78×10^{-3} are listed in Table 1. In general, the difference for $1000 \times (50 + 150)$ mesh and $800 \times (40 + 120)$ mesh is less than 0.9%, while the typical CPU time per time step for $1000 \times (50 + 150)$ mesh increases by a factor of 65%. Finally, the $800 \times (40 + 120)$ mesh is selected.

To validate this newly extended two-sided numerical model, firstly, a basic two-phase simulation without phase change performed by Liu et al. (1993) is compared through the specific case at $\Gamma = 4$, $\Pi = 1$, Pr = 1, Gr = 10^4, Ma = -100. The stream function computed by Liu et al. ranges in (−0.01375,1.565), the result computed by our simulation code

Table 1 Grid convergence for Nusselt numbers of hot and cold walls, maximum stream functions in liquid and gas phases, and maximum molar fraction of vapor

Grids-$Nx \times (Nz_l + Nz_g)$	Nu_c	Nu_h	$|\Psi_l|_{max}$	$|\Psi_g|_{max}$	$X_{v,\ max}$
$400 \times (20 + 60)$	2.824	2.366	2.908	4.799	0.05226
$600 \times (30 + 90)$	2.824	2.357	3.129	4.775	0.05239
$800 \times (40 + 120)$	2.826	2.348	3.236	4.769	0.05245
$1000 \times (50 + 150)$	2.825	2.342	3.305	4.763	0.05248

gives (−0.01351,1.596), where the relative difference is within ±2%. An additional check with experimental results is made by comparing present results with those given by Zhu and Liu (2010), see Fig. 2a. Average temperature gradient at the core region of the interface matches well while the temperature is slightly lower in their experiment on account that the cavity in their experiment is open to air, leading to larger interfacial temperature fall due to stronger evaporative cooling (without condensation). Finally, we compare the present result with Qin et al. (2014), in which the cavity is enclosed. Comparison is shown in Fig. 2b, the results are in good agreement except for a small discrepancy near the hot wall, which may due to the assumption of flat interface in the present work.

(a)

(b)
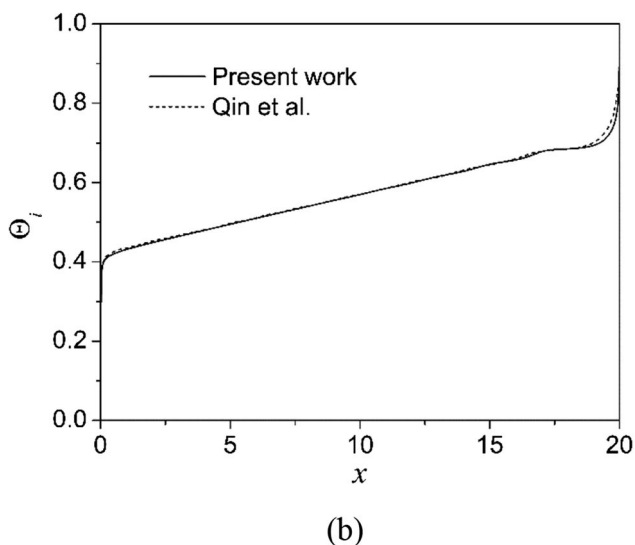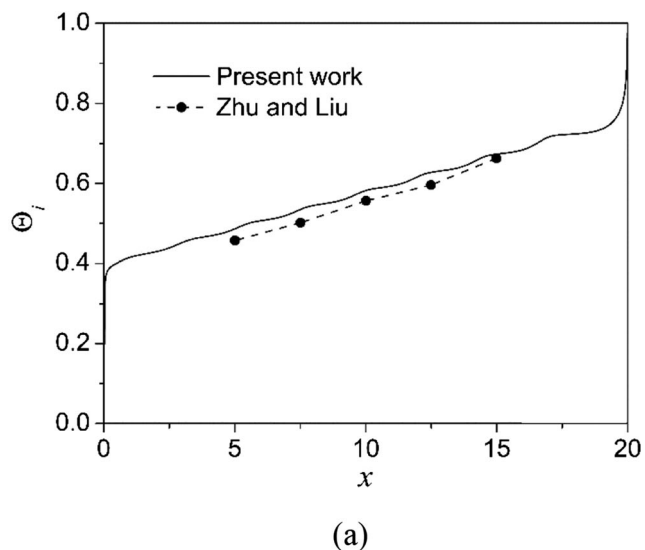
Fig. 2 Comparison of interfacial dimensionless temperature distribution between present work and **a** Zhu and Liu (2010) at $\Delta T = 10$ K, $H_l = 2$ mm **b** Qin et al. (2014) at $\Delta T = 10$ K, $H_l = 2.45$ mm

Results and Discussion

In the present study, we investigate the thermocapillary and buoyancy effects on natural thermo-convection of a volatile liquid contained in an enclosed cavity. 0.65 cSt silicone oil with a moderate Prandtl number, Pr = 6.83, is selected as the working liquid, and the gas layer is a component of air and liquid vapor, where air dominates. The physical properties of the liquid and gas at the reference temperature are listed in Table 2. The lateral walls are made of aluminium to strengthen heat conduction through the walls, where $\mathrm{Bi}_{w,\,l} = 2370$ and $\mathrm{Bi}_{w,\,g} = 9150$.

In most of the experimental studies, the test cell is fixed in geometry dimension, therefore the aspect ratio varies with different liquid layer depth, and it is usually out of consideration. However, Villers and Platten (1992) found that the number of convective rolls changes with the aspect ratio, Peltier and Biringen (1993) obtained the onset of oscillatory convection as a function of aspect ratio and Marangoni number. This experimental drawback can be overcome in numerical simulation. In this study, we fix $\Gamma = 20$, which is large enough to weaken the impact of lateral walls effect on interior flow structure. In addition, $\Pi = 3$ is selected following the work by Sáenz et al. (2013) which took into account the gas phase in their direct numerical simulations.

The mathematical approach for the choice of Marangoni number defined in (11) does not reflect the real physics, since the thermocapillary driven force is proportional to the horizontal temperature gradient $\Delta T/L$, rather than $\Delta T/H_l$. Therefore corrected laboratory Marangoni number will be introduced for results analysis, i.e.

$$\mathrm{Ma}_L = \frac{\sigma_T H_l^2}{\mu_l \alpha_l} \frac{\Delta T}{L} = \frac{\mathrm{Ma}}{\Gamma}. \qquad (38)$$

The strength of buoyancy convection is characterized by the Rayleigh number. To measure the relative strength of

Table 2 Physical properties of working liquid and air at $T_0 = 293$ K and $P_g = 1$ atm

	Liquid	gas
ρ (kg/m³)	761	1.205
μ (kg/m s)	4.95×10^{-4}	1.82×10^{-5}
α (m²/s)	9.52×10^{-8}	2.14×10^{-5}
k (W/m K)	0.1	2.59×10^{-2}
β (1/K)	1.34×10^{-3}	3.41×10^{-3}
σ (N/m)	1.59×10^{-2}	
σ_T (N/m K)	7×10^{-5}	
D (m²/s)	2.5×10^{-5}	
$P_{v,sat}$ (Pa)	4.4×10^3	
$\mathcal{L}$ (J/kg)	2.14×10^5	

buoyancy force to thermocapillary force, one should introduce the dynamic Bond number as

$$\mathrm{Bo} = \frac{\mathrm{Ra}}{\mathrm{Ma}} = \frac{\rho_l g \beta_l H_l^2}{\sigma_T}, \tag{39}$$

which only depends on the height of liquid layer.

Basic Characteristics of Steady Thermocapillary-Buoyancy Convection Coupled with Phase Change

Initially, fluids are at static state with uniform temperature T_0 and vapor is uniformly mixed with the air at $P_g = 1$ atm. Subjected to the imposed horizontal temperature gradient, fluids in both liquid phase and gas phase start to spontaneously flow counterclockwise and clockwise, respectively, which are driven by thermocapillary forces on the free interface and buoyancy force in the bulk. A steady return-flow basic state in liquid phase and gas phase shows up when the temperature gradient parallel with the interface is fully established for sufficiently low Ma_L. In particular, the case for a liquid layer at $\mathrm{Bo} = 0.6(H_l = 2$ mm$)$ and $\mathrm{Ma}_L = 149(\Delta T = 1$ K$)$ will be examined subsequently.

The flow structure is shown in Fig. 3. Convection is generally symmetric in the core region ($2 \le x \le 18$) of both liquid and gas phases and two so called "cat's-eye vortices" (Shevtsova et al. 2003) in the liquid layer are observed near the two end walls. Besides, the characteristics of temperature distribution in the cavity and along the interface are shown in Fig. 4. Driven by thermocapillary force, fluids close to the interface flow from the hot end to the cold end transporting the heated liquid and gas from right side to the left. Oppositely, fluids away from the interface return back from
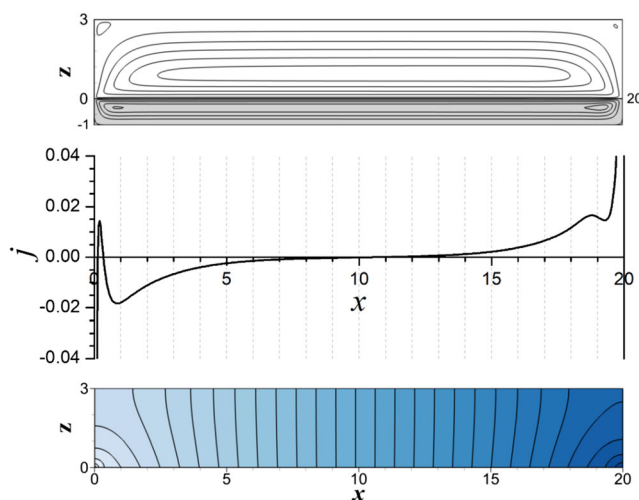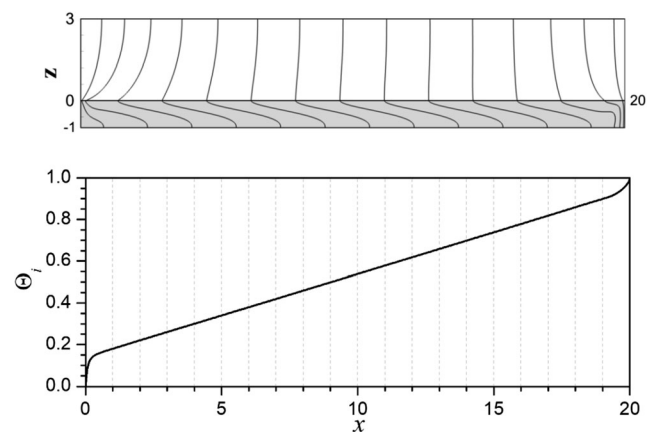
the hot end to the cold end. In this way, at the same location of x direction, liquid gets hotter upwards and gas gets hotter downwards. However, Prandtl number of gas is 0.7, which implies that thermal diffusion rate is larger than viscous diffusion rate in gas phase, so the gas gets hotter upwards near the hot wall. At the liquid-gas interface, temperature distributes linearly in the core region and temperature drops exist near the end walls.

Simultaneously, in the enclosed cavity with on-going phase change, evaporation and condensation lead to mass flux on the free liquid-gas interface which is shown in Fig. 3. Our primary interest is concentrated in the steady state of the flow, heat and mass transfer, thus the total net mass flux across the interface tends to zero (reaching global phase equilibrium) when the system comes to the quasi-static state. The Kinetic Theory of Gases (KTG) model (14), which is applicable when the system is slightly deviated from the thermodynamic equilibrium state (accurate at relatively small temperature difference i.e., steady state), together with mass conservation at the interface (28) are used to describe the mass flux across the interface. These two formulae represent non-equilibrium and diffusion-determined mechanisms of phase change, respectively. And the two mass fluxes j are consistent and they are associated with the interfacial temperature and partial pressure of vapor. In order to weigh the two mechanisms which control the phase change, a linearization of the two expressions is performed and deduced. It is assumed the vapor in air is dilute and the vapor mass fraction is tiny ($Y_v \ll 1$), so that $1 - Y_v \approx 1$, which yields $X_v \approx Y_v/r$ ($r = M_v/M_a$). Besides, the dimensionless z-direction gradient of the vapor mass fraction on the interface can be linearized with the mass fraction value of a nearby point ($Y_{v,n}$) that is just above the interface point, it gives:

$$\nabla Y_v \cdot \mathbf{n} = \frac{Y_{v,i} - Y_{v,n}}{\delta}, \tag{40}$$

where $Y_{v,i}$ is the interface mass fraction and $\delta = \Pi/Nz_g$ is the

Fig. 3 Flow field in cavity, liquid-gas interfacial dimensionless mass flux ($z = 0$) and molar fraction of vapor in gas phase at $\mathrm{Ma}_L = 149$ and $\mathrm{Bo} = 0.6$. Interval of the vapor molar fraction is $\delta X_v = 0.005\%$, darker region indicates higher molar fraction

Fig. 4 Temperature distribution in cavity and along liquid-gas interface ($z = 0$) at $\mathrm{Ma}_L = 149$ and $\mathrm{Bo} = 0.6$. Interval of the temperature in the cavity is $\delta \Theta = 0.065$

dimensionless distance (equals to the length scale of the unit grid) between the two points. Based on the above simplifications, (28) and (29) can be linearized as

$$E j = -\frac{\rho^* \nu^*}{Sc} \frac{Y_{v,i} - Y_{v,n}}{\delta}, \tag{41}$$

$$QE j = \bar{p}_{sat}(\Theta_i) - \frac{Y_{v,i}}{r}. \tag{42}$$

Combining (41) and (42) we find

$$\frac{Sc\delta}{r\rho^*\nu^*} E j = \frac{Y_{v,i}}{r} - \frac{Y_{v,n}}{r} \tag{43}$$

and

$$\left(Q + \frac{Sc\delta}{r\rho^*\nu^*}\right) E j = \bar{p}_{sat}(\Theta_i) - \frac{Y_{v,n}}{r}, \tag{44}$$

where $\frac{Y_{v,i}}{r}$ represents the simplified, dimensionless partial pressure of vapor at the liquid-gas interface. If we designate the dimensionless group in (42) and (43) as

$$R_n = QE, \tag{45}$$

$$R_d = \frac{Sc\delta E}{r\rho^*\nu^*}, \tag{46}$$

the mass flux j in (42), (43) and (44) can be written in the following form:

$$R_n j = p_{sat}(\Theta_i) - \frac{Y_{v,i}}{r}, \tag{47}$$

$$R_d j = \frac{Y_{v,i}}{r} - \frac{Y_{v,n}}{r}, \tag{48}$$

$$(R_n + R_d) j = p_{sat}(\Theta_i) - \frac{Y_{v,n}}{r}. \tag{49}$$

R_n and R_d correspond to the resistance to the phase transition triggered by interfacial non equilibrium and vapor transport, respectively. Take $\Delta T = 4$ K for example, if the average interfacial temperature $(T_c + T_h)/2 = 295$ K is assumed to be the value of T_i in dimensionless number Q and the height of the liquid layer is 2 mm, one finds $R_n = 2.87 \times 10^{-5}$ and $R_d = 4.98 \times 10^{-2}$, thus $R_d/R_n = 1.74 \times 10^3 \gg 1$. Therefore, R_n times j is a relatively small value, so is the difference between the interface saturation pressure and the interface vapor partial pressure $p_{sat}(\Theta_i) - Y_{v,i}/r$. In this way, the accuracy of the KTG model is validated in turn. Meanwhile, it can be concluded that it is the diffusion that dominates the phase change process. This is also why the two-sided approach is adopted in this simulation.

Vapor molar fraction is calculated through the mass diffusion-convection Eq. (7) together with Eq. (20) and the result is shown in Fig. 3. The sign of j can be easily estimated by the isolines of vapor molar fraction along with Eq. (48). It is apparent that vapor accumulates near the intersections between end walls and interface, where the interfacial vapor molar fraction gradient reaches the maximum. At the central region of the gas layer, the molar fraction is uniform in the vertical direction. One can find that the vapor molar fraction gradient along the interface dominates the mass flux distribution.

Interfacial mass flux of phase change (see Fig. 3) is strongly connected with the bulk flow in both liquid and gas phases. As expected, liquid evaporates in the hot region ($10.77 \leq x \leq 20$) and vapor condenses in the cold region ($0 \leq x < 0.13$ and $0.33 < x < 10.77$), however evaporation occurs at an unanticipated narrow part ($0.13 \leq x \leq 0.33$) near the cold wall, which is owing to the fast vapor evacuation caused by upward gas current. In addition, the maxima of condensational and evaporative mass flux away from the wall locate just above the center of two cat's-eye vortices.

Thermocapillary Effect

In the present section, we consider a liquid layer at a fixed dynamic Bond number Bo = 0.6, which corresponds to the liquid layer with a constant height $H_l = 2$ mm, thus thermocapillary effect weighs over buoyancy effect. Laboratory Marangoni number increases as the imposed temperature difference increases, which indicates the enhanced thermocapillary effect.

The streamlines at different imposed temperature difference when the flow reaches the steady state are shown in Fig. 5. The basic flow state at $\Delta T = 1$ K has been depicted previously. As temperature difference increases to $\Delta T = 4$ K, the cold end vortex in the liquid layer quickly merges with the core region, the roll near the hot end strengthens and two apparent counterclockwise rolls at the top gas layer corners appears as a result of buoyancy. Followed by Riley and Neitzel (1998) and Qin et al. (2014), it is referred to as steady unicellular flow (SUF).

At $\Delta T = 7$ K, three extra small rolls emerge near the hot wall in the liquid layer, and one clockwise roll, which is stronger than the rightmost one in liquid layer, separates from the uniformly rotative cell in the gas layer above the interface. At this time, flow regime in both layers corresponds to the steady multicellular flow (SMC). With ΔT increases, the rest of the uniform cells in both liquid and gas layers near the cold side splits into several independent rolls. When $\Delta T = 10$ K, the core region of two layers are fully developed, seven similar rolls in the liquid layer and five similar rolls in the gas layer are observed in the core regions, and the strength of those rolls gradually increases from cold side to hot side. The number of rolls in the system reaches maximum and two vortexes around the top corners in gas layer gradually strengthen due to the enhanced buoyancy effect in gas phase. At $\Delta T = 12$ K, the number of rolls in the liquid layer decreases and the flow
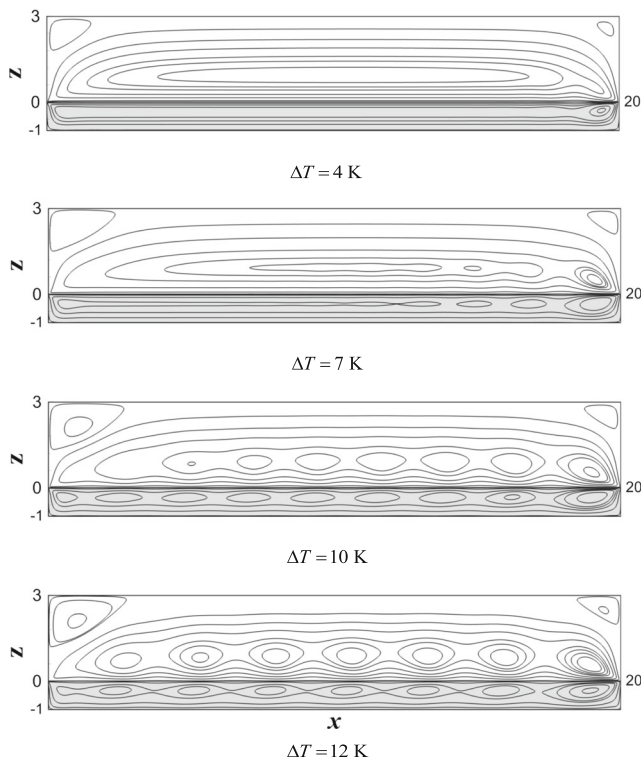
Fig. 5 Streamlines distribution of the steady flow for the imposed temperature difference $\Delta T = 4$, 7, 10 and 12 K at Bo = 0.6
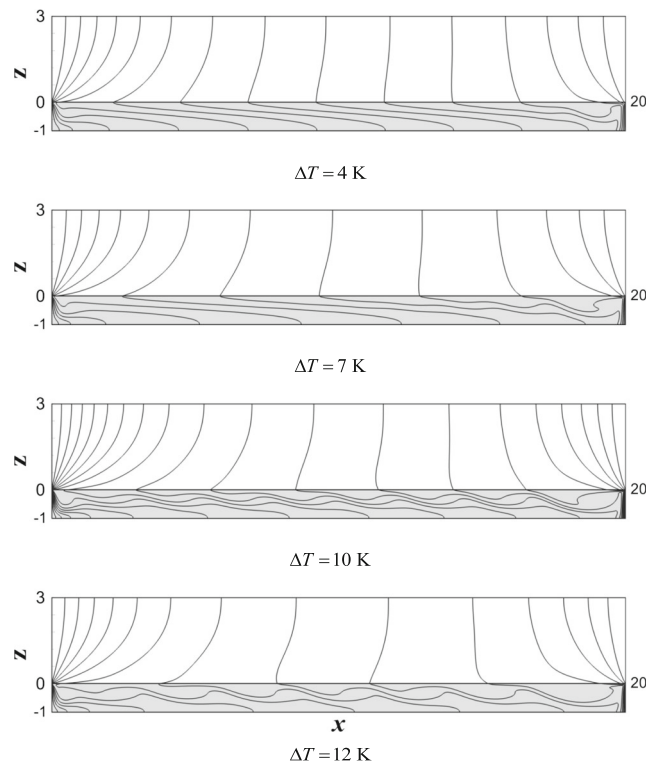
Fig. 6 Isotherms distribution of the steady flow for the imposed temperature difference $\Delta T = 4$, 7, 10 and 12 K at Bo = 0.6

comes to the nearly critical state of oscillating multicellular flow (OMC).

The trend of the temperature distribution in the bulk is associated with the flow patterns for different ΔT. Figure 6 shows the isotherms distribution at different ΔT when Bo = 0.6. As ΔT increases, isotherms become more intense near both hot and cold end walls, and in the liquid layer, isotherms fluctuate starting from the hot wall to the cold wall till $\Delta T = 10$ K when isotherms wave across the whole cavity. This trend is consistent with the development of liquid layer interior rolls.

Figure 7 shows the interfacial dimensionless temperature distribution. Thermocapillary convection is driven by the interfacial temperature gradient. Although the cavity is subjected to the imposed horizontal temperature gradient $\Delta T/L$, the experiment performed by Burguete et al. (2001) and numerical simulation by Sáenz et al. (2014) found that large interfacial temperature drop exists near the end walls. As a result, the actually working temperature gradient is much smaller than $\Delta T/L$ and the "effective interfacial Marangoni number" defined as

$$\mathrm{Ma}_i = \frac{\sigma_T H_l^2}{\mu_l \alpha_l} \left(\frac{\partial T_i}{\partial x} \right)_{core} \tag{50}$$

is introduced to eliminate the impact of temperature drops caused by lateral thermal boundary layers. Interfacial temperature gradient at the core region ($2 \leq x \leq 18$) is calculated by

linearly fitting the data. As shown in Fig. 7, we find that temperature drop at the cold wall is always larger than that at the hot wall and they both grow quickly with the increase of the imposed temperature difference. Besides, the thickness of the cold end thermal boundary layer is smaller compared to the hot end. Thus, the effective temperature gradient, which is the driving force of thermocapillary flow, reaches the largest near the hot wall. And this is why one finds the maximal stream function (see Fig. 11), either in gas phase or liquid phase, locates at the center of the cell adjacent to the hot wall
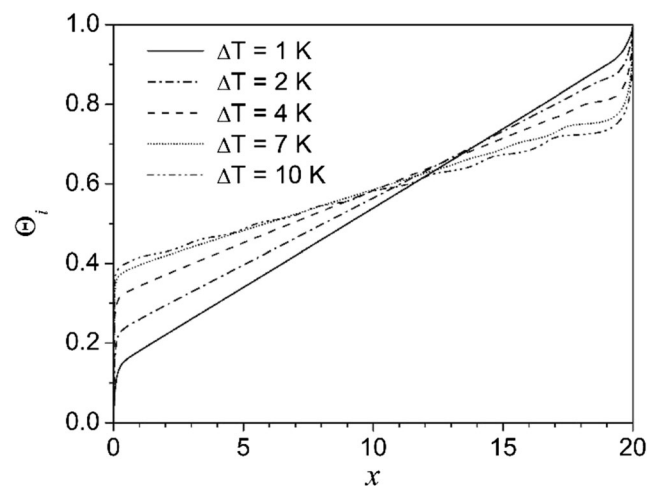
Fig. 7 Interfacial dimensionless temperature distribution for imposed temperature difference $\Delta T = 1$, 2, 4, 7, and 10 K at Bo = 0.6
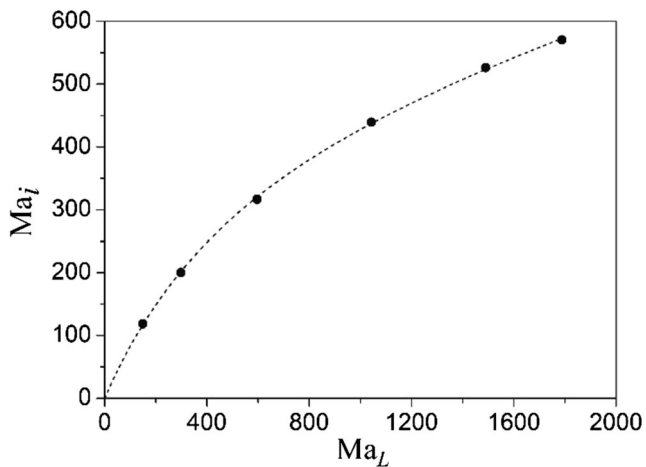
Fig. 8 Correlation between Ma_i and Ma_L (solid symbols) of steady thermo-convection for imposed temperature difference $\Delta T = 1, 2, 4, 7, 10$ and 12 K at Bo = 0.6. The dashed line is the fitting result as $Ma_i = Ma_L / \left(1.067 + 1.42 \times 10^{-3} Ma_L - 1.52 \times 10^{-7} Ma_L^2 \right)$

when Bo ≤ 2. Finally, we can correlate Ma_i with Ma_L, which is shown in Fig. 8.

On the liquid-gas interface, evaporation ($j > 0$) and condensation ($j < 0$) partly exist simultaneously. Figure 9 shows the interfacial dimensionless mass flux distribution at Bo = 0.6 for different imposed temperature differences. At the core region of the interface ($2 \leq x \leq 18$) where it is away from the lateral rigid walls, the mass transfer is immune to the boundary effect and strongly connected with the bulk flow patterns in the liquid phase. When $\Delta T \leq 4$ K, i.e. SUF state, only one uniform vortex exist in the core region of the liquid phase and the liquid adjacent to the free surface flows horizontally with no compensating vertical velocity caused by phase change, at the same time, the mass flux at that region is close to zero. As the imposed temperature difference increased, to SMC state, numbers of cells appear in the core region of the liquid layer and the mass flux fluctuates around the null point in this region. One can find that the mass flux distribution in the core region is consistent with the liquid flow patterns (Fig. 5). Take $\Delta T = 10$ K for instance, a sinusoidal mass flux distribution is formed in the core region of the interface with its seven troughs (maxima of condensational mass flux) and seven peaks (maxima of evaporative mass flux) located above the centers of the seven rolls and the interspace between two adjacent rolls, respectively. Moreover, the amplitude of the maximal evaporative or condensational mass flux is gradually amplified from the cold side to the hot side, which is consistent with the increasing vortex strength in the same orientation.

Besides, the mass flux close to the lateral walls is greatly affected by the boundary effect. Near the hot end, a condensational region exists and holds a span of the spatial wavelength of the rightmost liquid cells with its maximal mass flux -0.03 located at $x = 19.6$ for the imposed temperature difference $\Delta T \geq 4$ K. This unexpected condensational region is
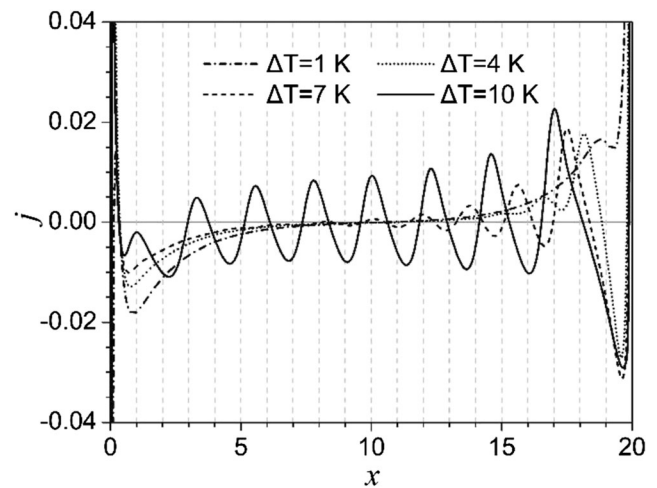

Fig. 9 Interfacial dimensionless mass flux for imposed temperature difference $\Delta T = 1, 4, 7$ and 10 K at Bo = 0.6

mainly caused by the downward gas current which accumulates the vapor near the interface to make the vapor partial pressure larger than the local saturated vapor pressure. On the contrary, liquid evaporates into vapor near the hot wall at $\Delta T = 1$ K. This is mainly on account that the flow in liquid layer is weak, therefore the heat transfer is dominated by diffusion rather than advection, so that heat transfer from the hot to the cold side near the hot end is poor near the interface which makes the interfacial temperature T_i higher than the corresponding saturation temperature T_s (this can be verified
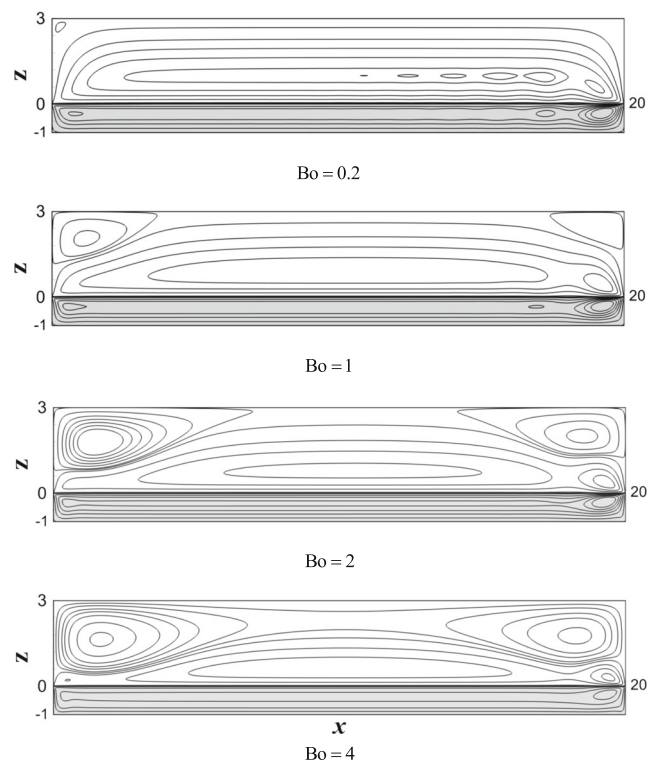
Fig. 10 Streamlines distribution of the steady flow for the dynamic Bond number Bo = 0.2, 1, 2 and 4 at $Ma_L = 868$
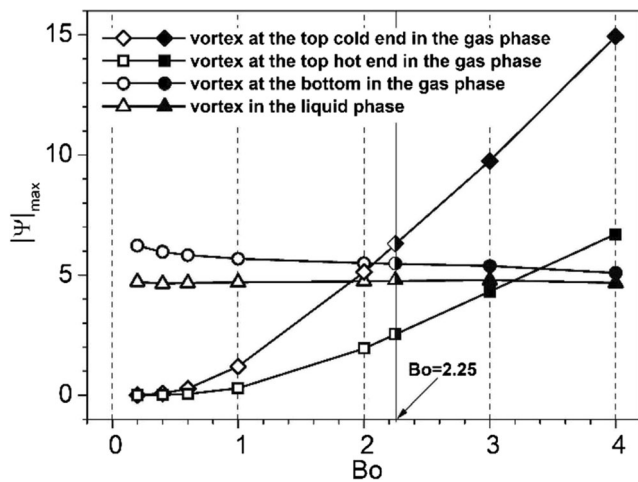
Fig. 11 The maximum dimensionless stream function $|\Psi|_{max}$ versus the dynamic Bond numbers in the liquid phase (triangles) and the three vortexes which are located at the bottom (circles), the top cold end (diamonds) and the top hot end (squares) in the gas phase, respectively. The vertical solid line shows transitions between monolayer flow and multilayer flow in the gas phase. Open and solid symbols correspond to monolayer gas flow and multilayer gas flow, respectively

in Fig. 6 if we compare the isotherms between $\Delta T = 1$ K and $\Delta T = 10$ K). Close to the right wall, liquid evaporates in a very narrow region ($19.8 < x < 20$), for the imposed wall temperature is the highest one in the whole system which is expected to be higher than the local T_s. Analogously, near the cold end, vapor condenses except for the region $0.1 < x < 0.4$, where the interfacial temperature increases rapidly from the cold wall (see Fig. 7), and the vapor is transported away from the interface due to the upward gas current.

Buoyancy Effect

The relative weight of Buoyancy effect to thermocapillary effect is determined by the dynamic Bond number. To illustrate the impact of buoyancy effect on flow patterns, energy transport and phase-change flux, three sets of different dynamic Bond numbers, corresponding to the low (Bo = 0.2), the moderate (Bo = 1) and the high (Bo = 2 and 4), are examined at a fixed laboratory Marangoni number $Ma_L = 868$, which is moderate to ensure the system maintain the steady state.

In Fig. 10, the liquid layer is shallow at Bo = 0.2($H_l = 1.18$ mm). Buoyancy plays a minor impact on the bulk flow and the liquid layer is at the steady partial multicellular flow (PMC) state, which is defined by Li et al. (2014). A small roll shows up adjacent to the cell near the hot wall, it has a shorter wave length and is far weaker than the latter. Riley and Neitzel (1998) reported in their experiment that the transition from the SUF to the hydrothermal-wave instability occurs when Bo ≤ 0.22($H_l ≤ 1.25$ mm), and the flow in the liquid layer will be at the unicellular basic state whether it is steady or not. In our simulation, no SMC state is found before the onset of hydrothermal waves at Bo = 0.2. This is in consistent with Riley and
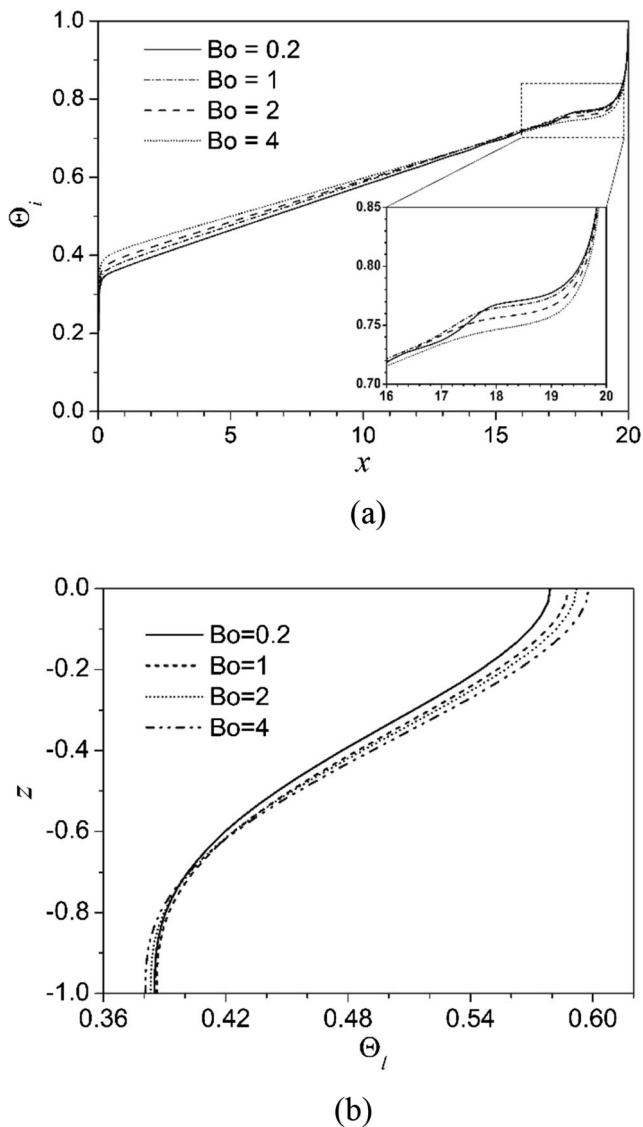
Neitzel (1998), yet the existence of PMC is mainly on account that the Prandtl number in their experiment is double of ours. At Bo = 1($H_l = 2.65$ mm), the buoyancy effect balances the thermocapillary effect. PMC state, which is mainly caused by the thermocapillary effect, still exists in the liquid layer, while two cells in the gas layer emerge at the top corners due to the enhanced buoyancy effect.

As Bo is increased to Bo ≥ 2, the rolls near the cold end and adjacent to the rightmost cell gradually merge with the liquid bulk flow, thus the flow state degenerates from the PMC to SUF state. The wave length of the rightmost cell in the liquid layer decreases and the flow in the core region tends to be uniform. We find that the maximum stream function of the liquid layer always locates at the center of the rightmost cell near the hot wall, as shown in Fig. 11, it remains almost the same when dynamic Bond number varies. However, on the median plane of the liquid layer, the maximum horizontal velocity (U_l) of the return flow from the cold end to hot end increases as the buoyancy effect strengthens (see Fig. 12). It can be concluded that the increasing buoyancy effect accelerates the liquid bulk flow which makes the flow field simple and uniform.

In gas phase, the flow pattern is easily transformed with the increasing buoyancy effect. At Bo < 1, the vortex strength of the cells occupying the top cold and hot walls grow slowly with the increasing Bo. When buoyancy weighs over thermocapillary, that is Bo > 1, the maximum stream function $|\Psi|_{max}$ of those two vortexes at the gas phase top corner grows linearly with the increasing Bo. These observations are shown in Fig. 11. For the first time we are reporting the two-layer flow patterns in the gas phase above the phase-change liquid-gas interface, see Fig. 10 (Bo = 4), and the critical dynamic Bond number dividing the steady monolayer gas flow into multilayer gas flow is found to be 2.25. This critical value is
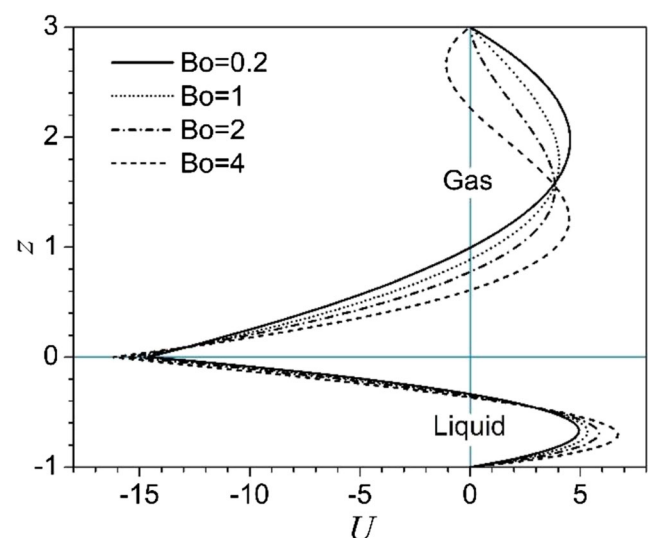
Fig. 12 Vertical profile of dimensionless horizontal velocity U on the median plane ($x = 10$) at $Ma_L = 868$ for Bo = 0.2, 1, 2 and 4
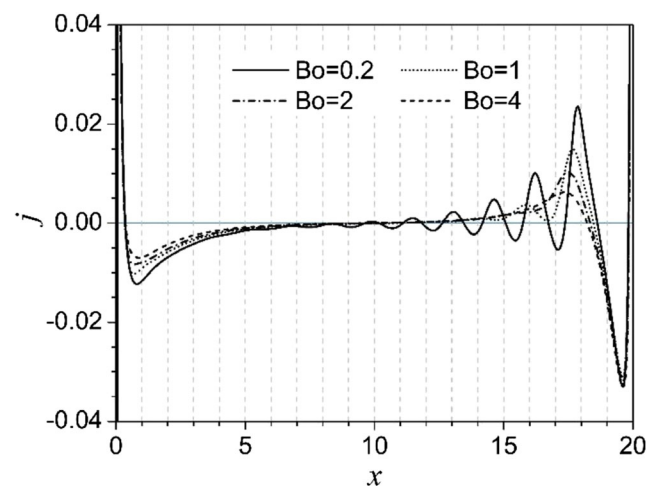
(a)

(b)

Fig. 13 Dimensionless temperature distribution of **a** interface, **b** vertical median plane in the liquid layer for Bo = 0.2, 1, 2 and 4 at Ma_L = 868. Inset in **a**: partial enlarged image near the hot end
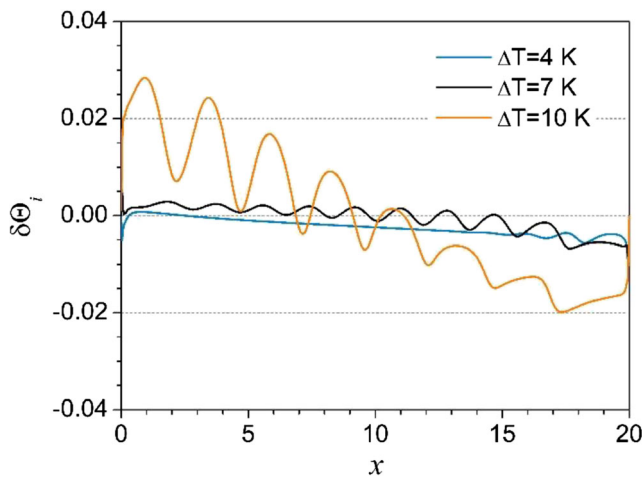
strength of rightmost cells next to the interface, even if when buoyancy effect dominates.

Figure 13a shows the interfacial dimensionless temperature distribution for different dynamic Bond numbers at Ma_L = 868. As we already mentioned, the thickness of the thermal boundary layers and temperature drops at the end walls are greatly influenced by the Marangoni numbers, so are they affected by dynamic Bond numbers. Larger Bo corresponds to thicker thermal boundary layers at the hot wall and larger temperature drops at both hot and cold walls. Figure 13b shows the vertical median dimensionless temperature distribution in the liquid layer. When Bo increases, the vertical temperature gradient at $-0.6 < z < -0.2$ increases. These are consistent with Burguete et al. (2001) who reported that when H_l increases, ω_H/ω_I, namely the ratio of effective horizontal temperature gradient ($\omega_H = \partial T_i/\partial x|_{core}$)to the imposed temperature gradient ($\omega_I = \Delta T/L$), decreases continuously, while $\omega_V = \partial T_l/\partial y|_{median}$, namely the vertical temperature gradient in liquid layer, increases.

Figure 14 shows the mass flux distribution for different dynamic Bond numbers. A tight connection between the mass flux and the liquid flow pattern is validated further. Though all cases in Fig. 14 are at Ma_L = 868 and the maximal stream functions in the liquid phase stay almost the same, the flow patterns transform from SMC to PMC to SUF with the increasing Bo, which implies that the number of cells decreases and the flow velocity near the interface tends to be more uniform and horizontal in the core region of liquid layer. At the same time, the fluctuation of the mass distribution in the central part recedes to null as Bo increases. The remaining region close to the cold and hot walls has the similar distribution as we elucidated in Fig. 9.

searched by means of the horizontal velocity U_g on the median plane when it turns to be negative at the upper layer, see Fig. 12 (Bo = 4). Open and solid symbols in Fig. 11 correspond to monolayer gas flow and multilayer gas flow, respectively. With the increasing Bo, two cells at the top gas corners grow stronger and larger, and finally merge at the center of the gas layer top side. Noted that the maximum stream function of the bottom gas layer (circles in Fig. 11) locates at the center of the rightmost cell near the hot wall and remains almost unchanged with the increasing Bo. Together with variation of the counterpart in the liquid layer (triangles in Fig. 11), we can conclude that thermocapillary force plays a leading role in the

Fig. 14 Interfacial dimensionless mass flux for dynamic Bond number Bo = 0.2, 1, 2 and 4 at Ma_L = 868

Fig. 15 Profile of dimensionless interfacial temperature difference between phase-change model and none phase-change model for imposed temperature difference $\Delta T = 4$, 7 and 10 K at Bo $= 0.6$. $\delta\Theta_i$ equals interfacial temperature of phase-change model minus that of none phase-change model

Phase-Change Effect

In order to investigate the impact of phase change on thermo-convection, the case of pure buoyancy-thermocapillary convection without phase change ($j = 0$ on the interface and $Y_v = 0$ in gas phase) at Bo $= 0.6$ is examined and compared with the corresponding cases with phase change on.

Not only the convection and the heat transfer have an impact on the mass flux at the interface, the latent heat absorbed or released when phase change happens can alter the interfacial temperature distribution in turn. Figure 15 shows the interfacial temperature difference between phase-change model and corresponding no phase-change case. Evaporative cooling effect concentrates in the region near the hot wall and condensational heating effect concentrates in the region near the cold
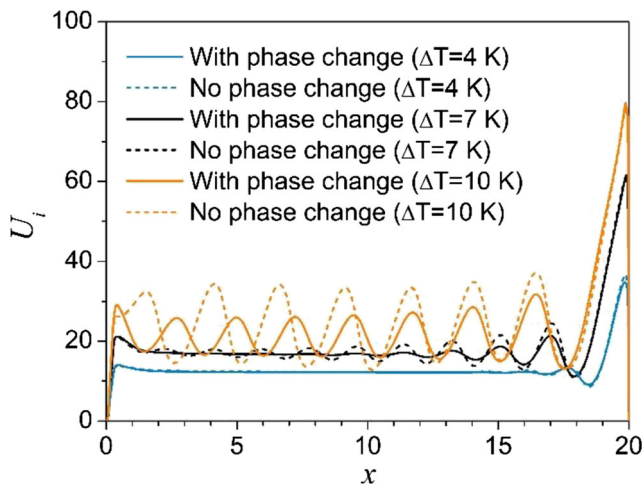
Fig. 16 Interfacial horizontal dimensionless velocity U_i for imposed temperature difference $\Delta T = 4$, 7 and 10 K at Bo $= 0.6$ with phase change (solid line) and without phase change (dashed line)
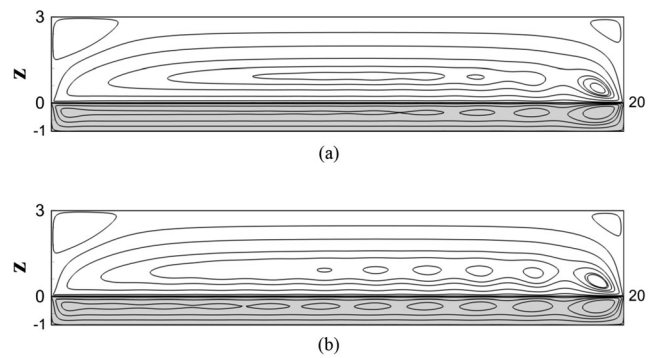
Fig. 17 Streamlines distribution of **a** phase-change model **b** no phase-change model for the imposed temperature difference $\Delta T = 7$ K at Bo $= 0.6$

wall. In general, for larger imposed temperature difference, the variation of interfacial temperature will be larger and the condensational heating region is larger.

Consequently, the average effective temperature gradient on the interface decreases due to the phase-change effect, which can lead to a decrease on interfacial thermocapillary force. Figure 16 shows the interfacial horizontal velocity using two different models. At $\Delta T = 4$ K, tiny difference can be found between two models. For larger ΔT, interfacial horizontal velocity fluctuates in core region due to the convective cells in liquid layer, and the amplitudes of the fluctuations are apparently larger in cases without phase change. Figure 17 shows the streamlines distribution of phase-change case and no phase-change case at $\Delta T = 7$ K and Bo $= 0.6$. More rolls in the core region are found in the no phase-change case, which is due to the stronger thermocapillary effect. These observations imply that phase change play a stabilizing role in the thermocapillary-buoyancy flow.

Conclusions

We have presented numerical simulations on steady thermocapillary-buoyancy convection in an enclosed cavity subjected to horizontal temperature gradient. A two-phase model which fully accounts for diffusion-convection transport of vapor has been developed. Combined kinetic theory of gases and vapor-diffusion-limited mechanism has been used for phase change and the latter is validated to play a dominating role. The Numerical model has been compared with other experimental and numerical works, and results are in good agreement.

We find thermocapillary effect has a strong impact on flow patterns of the liquid layer. As the imposed temperature gradient (i.e. Marangoni number) is increased, steady unicellular flow turns into steady multicellular flow with the number of rolls gradually increasing and finally decreasing when the flow is about to oscillate, and isotherms start to fluctuate from the hot to the cold wall due to the emergence of rolls.

Buoyancy effect has a major impact on flow pattern of the gas layer. As the dynamic Bond number is increased, the bulk flow accelerates and the convection in gas layer is separated into a two-layer flow. Near the hot and cold walls, thermal boundary layer gives rise to interfacial temperature drops, which are always larger at the cold end, and they both increase as the imposed temperature gradient and the dynamic Bond number are increased. Effective interfacial Marangoni number is defined to reflect the actually working temperature gradient at the interface and a correlation with laboratory Marangoni number is given.

Interfacial phase-change flux has also been investigated. We find the distribution of mass flux is strongly associated with the flow patterns in the liquid layer. Evaporation and condensation occur alternately in the core region at multicellular flow state, and it has the same wavelength as the corresponding convective rolls in the liquid layer. Interestingly, a part of evaporation near the cold wall and a part of condensation near the hot wall are observed. This boundary effect could be explained by the vapor evacuation due to upward gas current near the cold end and vapor accumulation due to downward gas return flow near the hot end, together with the temperature drops at cold and hot walls. In order to investigate the phase-change effect, a corresponding model ignoring phase change and vapor transport has been performed as a reference. The latent heat absorbed at the evaporative regions and released at the condensational regions can decrease the interfacial temperature gradient, consequently, thermocapillary force is weaken. In other words, phase change tends to stabilize the thermocapillary-buoyancy flows.

References

Abe, Y., Iwaski, A., Tanaka, K.: Thermal management with self-rewetting fluids. Microgravity Sci. Technol. **16**, 148–152 (2005). https://doi.org/10.1007/BF02945966

Bekezhanova, V.B., Goncharova, O.N.: Thermocapillary convection with phase transition in the 3D channel in a weak gravity field. Microgravity Sci. Technol. **31**, 1–20 (2019)

Bénard, H.: Les tourbillons cellulaires dans une nappe liquide. Rev. Gen. Sci. Pures Appl. **11**, 1261–1271 (1900)

Brutin, D., Zhu, Z.Q., Rahli, O., et al.: Evaporation of ethanol drops on a heated substrate under microgravity conditions. Microgravity Sci. Technol. **22**(3), 387–395 (2010)

Burelbach, J.P., Bankoff, S.G., Davis, S.H.: Nonlinear stability of evaporating/condensing liquid films. J. Fluid Mech. **195**, 463–494 (1988). https://doi.org/10.1017/S0022112088002484

Burguete, J., Mukolobwiez, N., Daviaud, F., Garnier, N., Chiffaudel, A.: Buoyant-thermocapillary instabilities in extended liquid layers subjected to a horizontal temperature gradient. Phys. Fluids. **13**, 2773–2787 (2001). https://doi.org/10.1063/1.1398536

Cecere, A., Di Martino, G.D., Mungiguerra, S.: Experimental investigation of capillary-driven two-phase flow in water/Butanol under reduced gravity conditions. Microgravity Sci. Technol. **31**(4), 425–434 (2019)

Chai, A.T., Zhang, N.: Experimental study of Marangoni-Bénard convection in a liquid layer induced by evaporation. Exp. Heat Transf. **11**, 187–205 (1998). https://doi.org/10.1080/08916159808946561

Chan, C.L., Chen, C.F.: Effect of gravity on the stability of thermocapillary convection in a horizontal fluid layer. J. Fluid Mech. **647**, 91–103 (2010). https://doi.org/10.1017/S0022112009994046

Chen, P.C., Lin, W.K.: The application of capillary pumped loop for cooling of electronic components. Appl. Therm. Eng. **21**, 1739–1754 (2001). https://doi.org/10.1016/S1359-4311(01)00045-X

Chen, X., Zhu, Z.Q., Liu, Q.S., et al.: Thermodynamic behaviors of macroscopic liquid droplets evaporation from heated substrates. Microgravity Sci. Technol. **27**(5), 353–360 (2015)

Chen, X., Wang, X., Chen, P.G., et al.: Thermal effects of substrate on Marangoni flow in droplet evaporation: response surface and sensitivity analysis. Int. J. Heat Mass Transf. **113**, 354–365 (2017)

Chen, X., Wang, X., Chen, P.G., et al.: Determination of diffusion coefficient in droplet evaporation experiment using response surface method. Microgravity Sci. Technol. **30**(5), 675–682 (2018)

Derby, J.J.: Fluid dynamics in crystal growth: the good, the bad, and the ugly. Prog. Cryst. Growth Charact. Mater. **62**, 286–301 (2016). https://doi.org/10.1016/j.pcrysgrow.2016.04.015

Haut, B., Colinet, P.: Surface-tension-driven instabilities of a pure liquid layer evaporating into an inert gas. J. Colloid Interface Sci. **285**, 296–305 (2005). https://doi.org/10.1016/j.jcis.2004.07.041

Ji, Y., Liu, Q.S., Liu, R.: Coupling of evaporation and thermocapillary convection in a liquid layer with mass and heat exchanging interface. Chin. Phys. Lett. **25**, 608–611 (2008). https://doi.org/10.1088/0256-307X/25/2/069

Li, Y., Grigoriev, R., Yoda, M.: Experimental study of the effect of non-condensables on buoyancy-thermocapillary convection in a volatile low-viscosity silicone oil. Phys. Fluids. **26**, 122112 (2014). https://doi.org/10.1063/1.4904870

Liu, R., Liu, Q.S.: Linear stability analysis of convection in two-layer system with an evaporating vapor-liquid interface. Acta Mech. Sinica. **22**, 109–119 (2006). https://doi.org/10.1007/s10409-006-0106-6

Liu, Q.S., Chen, G., Roux, B.: Thermogravitational and thermocapillary convection in a cavity containing two superposed immiscible liquid layers. Int. J. Heat Mass Transf. **36**, 101–117 (1993). https://doi.org/10.1016/0017-9310(93)80070-B

Liu, M., Ren, Y.X., Zhang, H.: A class of fully second order accurate projection methods for solving the incompressible Navier-stokes equations. J. Comput. Phys. **200**, 325–346 (2004). https://doi.org/10.1016/j.jcp.2004.04.006

Liu, R., Liu, Q.S., Hu, W.R.: Marangoni–Bénard instability with the exchange of evaporation at liquid-vapour interface. Chin. Phys. Lett. **22**, 402–404 (2005). https://doi.org/10.1088/0256-307X/22/2/037

Margerit, J., Dondlinger, M., Dauby, P.C.: Improved 1.5-sided model for the weakly nonlinear study of Bénard–Marangoni instabilities in an evaporating liquid layer. J. Colloid Interface Sci. **290**, 220–230 (2005). https://doi.org/10.1016/j.jcis.2005.04.031

Mo, D.M., Ruan, D.F.: Linear-stability analysis of Thermocapillary-buoyancy convection in an annular two-layer system with upper rigid wall subjected to a radial temperature gradient. Microgravity Sci. Technol. **31**(3), 293–304 (2019)

Nield, D.A.: Surface tension and buoyancy effects in cellular convection. J. Fluid Mech. **19**, 341–352 (1964). https://doi.org/10.1017/S0022112064000763

Palmer, H.J.: The hydrodynamic stability of rapidly evaporating liquids at reduced pressure. J. Fluid Mech. **75**, 487–511 (1976). https://doi.org/10.1017/S0022112076000347

Pearson, J.R.A.: On convection cells induced by surface tension. J. Fluid Mech. **4**, 489–500 (1958). https://doi.org/10.1017/S0022112058000616

Peltier, L.J., Biringen, S.: Time-dependent thermocapillary convection in a rectangular cavity: numerical results for a moderate Prandtl number fluid. J. Fluid Mech. **257**, 339–357 (1993). https://doi.org/10.1017/S0022112093003106

Qin, T., Tuković, Ž., Grigoriev, R.O.: Buoyancy-thermocapillary convection of volatile fluids under atmospheric conditions. Int. J. Heat Mass Transf. **75C**, 284–301 (2014). https://doi.org/10.1016/j.ijheatmasstransfer.2014.03.027

Riley, R.J., Neitzel, G.P.: Instability of thermocapillary-buoyancy convection in shallow layers. Part 1. Characterization of steady and oscillatory instabilities. J. Fluid Mech. **359**, 143–164 (1998). https://doi.org/10.1017/S0022112097008343

Sáenz, P.J., Valluri, P., Sefiane, K., Karapetsas, G., Matar, O.K.: Linear and nonlinear stability of hydrothermal waves in planar liquid layers driven by thermocapillarity. Phys. Fluids. **25**, 094101 (2013). https://doi.org/10.1063/1.4819884

Sáenz, P.J., Valluri, P., Sefiane, K., Karapetsas, G., Matar, O.K.: On phase change in Marangoni-driven flows and its effects on the hydrothermal-wave instabilities. Phys. Fluids. **26**, 024114 (2014). https://doi.org/10.1063/1.4866770

Schmidt, G.R., Chung, T.J., Nadarajah, A.: Thermocapillary flow with evaporation and condensation at low gravity. Part 1. Non-deforming surface. J. Fluid Mech. **294**, 323–347 (1995)

Schrage, R.W.: A theoretical study of interface mass transfer. Columbia University Press, New York (1953)

Shevtsova, V.M., Nepomnyashchy, A.A., Legros, J.C.: Thermocapillary-buoyancy convection in a shallow cavity heated from the side. Phys. Rev. E. **67**, 066308 (2003). https://doi.org/10.1103/PhysRevE.67.066308

Simanovskii, I., Viviani, A., Dubois, F., et al.: Nonlinear convective flows in a laterally heated two-layer system with a temperature-dependent heat release/consumption at the interface. Microgravity Sci. Technol. **30**(3), 243–256 (2018)

Smith, M.K., Davis, S.H.: Instabilities of dynamic thermocapillary liquid layers. Part 1. Convective instabilities. J. Fluid Mech. **132**, 119–144 (1983). https://doi.org/10.1017/S0022112083001512

Swarztrauber, P.N.: The methods of cyclic reduction, Fourier analysis and the FACR algorithm for the discrete solution of Poisson's equation on a rectangle. SIAM Rev. **19**, 490–501 (1977)

Villers, D., Platten, J.K.: Coupled buoyancy and Marangoni convection in acetone experiments and comparison with numerical simulations. J. Fluid Mech. **234**, 487–510 (1992). https://doi.org/10.1017/S0022112092000880

Wang, X., Liu, Q., Zhu, Z., et al.: Experiments of transient condensation heat transfer on the heat flux senor. Microgravity Sci. Technol. **27**(5), 369–376 (2015)

Zhang, L., Li, Y.R.: Three-dimensional numerical simulation on Thermocapillary convection of moderate Prandtl number fluid in an annular shallow Pool with surface heat dissipation. Microgravity Sci. Technol. 1–15 (2019), 31(6):733–747. https://doi.org/10.1007/s12217-019-9704-3

Zhang, L., Li, Y.R., Wu, C.M.: Effect of surface evaporation on steady thermocapillary convection in an annular pool. Microgravity Sci. Technol. **28**, 499–509 (2016). https://doi.org/10.1007/s12217-016-9510-0

Zhang, Y., Li, Y.R., Yu, J.J., et al.: Three-dimensional numerical simulation on Marangoni convection in a sessile water droplet evaporating in its vapor at low pressure. Microgravity Sci. Technol. **31**(2), 231–240 (2019)

Zhu, Z.Q., Liu, Q.S.: Coupling of thermocapillary convection and evaporation effect in a liquid layer when the evaporating interface is open to air. Chin. Sci. Bull. **55**, 233–238 (2010). https://doi.org/10.1007/s11434-009-0693-2

Zhu, Z.Q., Brutin, D., Liu, Q.S., et al.: Experimental investigation of pendant and sessile drops in microgravity. Microgravity Sci. Technol. **22**(3), 339–345 (2010)